



## Dynamic Hepatocellular Carcinoma Model Within a Liver Phantom for Multimodality Imaging

Muntaser S. Ahmad<sup>a,\*</sup>, Nursakinah Suardi<sup>a</sup>, Ahmad Shukri<sup>a</sup>, Nik Noor Ashikin Nik Ab Razak<sup>a</sup>, Ammar A. Oglat<sup>b</sup>, Osama Makhamrah<sup>c</sup>, Hjouj Mohammad<sup>c</sup>

<sup>a</sup> School of Physics, Universiti Sains Malaysia, 11800, Penang, Malaysia

<sup>b</sup> Department of Medical Imaging, Faculty of Applied Medical Sciences, Hashemite University, Zarqa, Jordan

<sup>c</sup> Medical Imaging Department, Faculty of Health Professions, Al-Quds University, Jerusalem, Palestine

### ARTICLE INFO

#### Keywords:

Liver phantom  
Dynamic phantom  
HCC  
CT  
MRI

### ABSTRACT

**Introduction:** Hepatocellular carcinoma (HCC) is one of the most common cancer in the world, and the effectiveness of its treatment lies in its detection in its early stages. The aim of this study is to mimic HCC dynamically through a liver phantom and apply it in multimodality medical imaging techniques including magnetic resonance imaging (MRI), computed tomography (CT), and ultrasound.

**Methods and materials:** The phantom is fabricated with two main parts, liver parenchyma and HCC inserts. The liver parenchyma was fabricated by adding 2.5 wt% of agarose powder combined with 2.6 wt% of wax powder while the basic material for the HCC samples was made from polyurethane solution combined with 5 wt% glycerol. Three HCC samples were inserted into the parenchyma by using three cylinders implanted inside the liver parenchyma. An automatic injector is attached to the input side of the cylinders and a suction device connected to the output side of the cylinders. After the phantom was prepared, the contrast materials were injected into the phantom and imaged using MRI, CT, and ultrasound.

**Results:** Both HCC samples and liver parenchyma were clearly distinguished using the three imaging modalities: MRI, CT, and ultrasound. Doppler ultrasound was also applied through the HCC samples and the flow pattern was observed through the samples.

**Conclusion:** A multimodal dynamic liver phantom, with HCC tumor models have been fabricated. This phantom helps to improve and develop different methods for detecting HCC in its early stages.

### 1. Introduction

Differentiating between normal and pathological tissues is the basis for medical imaging modalities. Medical imaging technology is best if it is able to detect the difference between these tissues during the different stages of a disease. One of the most important diseases to be detected in its early stages is hepatocellular carcinoma (HCC).

HCC is the most common type of primary liver cancer, and is the most common cause of death among different cancers after lung cancer [1–3]. This cancer can be diagnosed using various modalities including ultrasound [4], computed tomography (CT) [5,6], and magnetic resonance imaging (MRI) [7,8]. The ability of these modalities to diagnose HCC is differentiated in its different stages where MRI is the best modality in diagnosing this disease. However, all three modalities suffer from limitations of detection of HCC in its early stages [9–11].

In clinical practices, the detection of HCC in early-stage cancer is one of the greatest challenges facing radiologists. Through this scenario, we need an alternative to human tissue to facilitate the development of imaging systems in the early detection of HCC instead of conducting clinical trials directly on patients. A dynamic liver phantom can be used as one of the alternatives to achieving this goal. This phantom should include liver parenchyma and locations of HCC samples within this parenchyma.

Liver phantoms are commercially available and have been described in the literature. There are many companies providing training models and image-guided navigation technology in commercial liver phantoms. One of these companies is Computerized Imaging Reference Systems, Incorporated (CIRS) a manufacturer of tissue equivalent phantoms and simulators for medical imaging, radiation therapy and procedural training for tissue simulation and phantom technology [12]. It supplies

\* Corresponding author.

E-mail address: [wmuntaser@gmail.com](mailto:wmuntaser@gmail.com) (M.S. Ahmad).

<https://doi.org/10.1016/j.ejro.2020.100257>

Received 20 June 2020; Accepted 24 August 2020

2352-0477/© 2020 The Author(s). Published by Elsevier Ltd.

This is an open access article under the CC BY-NC-ND license

(<http://creativecommons.org/licenses/by-nc-nd/4.0/>).



Fig. 1. The liver phantom mold; (a): Anterior surface; (b): Posterior surface.

the Triple Modality 3D Abdominal Phantom. Another company supplies the IOUSFAN® phantom [13] which provides a representation of upper abdominal organs (Kyoto Kagaku Co., Ltd, Kyoto, Japan), whilst another company, QRM GmbH supplies another version of a semi-anthropomorphic liver phantom (QRM-Abdomen Phantom, QRM GmbH, Möhrendorf, Germany) which can be used in CT for the examination of low contrast details in the liver region [14]. These companies supply phantoms with a realistic appearance and provide tumor models with blood vessel structures.

The liver phantom can be made using several different tissue-mimicking materials that are compatible with the imaging modalities [15]. Most of the liver phantoms were developed for applications in CT imaging [16–23], while far less phantoms were intended for MRI [24–26] and ultrasound [27–30]. However, multimodal liver phantoms which can be applied under different medical imaging modalities including MRI, CT, and ultrasound are still less developed [12,24,31].

The most common substances used for liver phantom fabrication are polyacrylamide (PAA), carrageenan, polysaccharide, agar, agarose [24, 27], polyvinyl alcohol (PVA) [32], polyurethane [31], gelatin [33,34] and silicone, commercial rigid plastics [35], and elastomeric (rubber-like) materials [36].

There are quite a number of liver phantoms proposed and described in the scientific literature or available in the market which describes the blood vessel structures, model tumors [24,27,31], and provide blood flow functionality [31]. However, none of them provide flow functionality through tumors like HCC. This study aims to fabricate a phantom which simulates both the liver parenchyma of a real human, and HCC in its typical pattern, to produce realistic images through medical imaging modalities including MRI, CT, and ultrasound. The phantom must be prepared with the ability to alter HCC samples without affecting liver parenchyma. In the next section, experimental steps are described to produce the dynamic phantom for dynamic imaging through the different medical imaging modalities.

## 2. Materials and methods

The presented multimodal liver phantom contains three components: the largest part of phantom corresponding to the liver tissue (parenchyma), the second part refers to the flow part (representing blood vessels) and the third part refers to HCC samples.

The location of the second part of the phantom is intra-parenchyma (from superior to inferior surfaces of the phantom). The input unit enters the phantom from the superior surface of the liver phantom while the output unit exits from the inferior surface of the liver phantom. All the parts are connected to each other to form one unit.

The blood vessels in the phantom consist of two parts: the input unit and output unit. The input part is directly connected to the automatic injector while the output unit is directly connected to the suction device. Both the input and output units are connected to each other through a cylindrical medium that have different sizes and they contain HCC samples. Each of these cylinders contain a certain size of HCC, which is

different than that found in other cylinders.

The flow of contrast agent (CA) into the mold is created by attaching the automatic injector to the input unit using a medical connecting tube. After injecting the CA into the cylinder, it interacts with the pathological sample (HCC), after which the CA will be sucked out from the phantom by a suction device connected directly to the output unit. The flow rate and the suction power were determined by setting the automatic injector at 2 mL/s using the power Injector (Spectris Solaris EP MR, MEDRAD®) and the suction device by setting it to the suction power 26 L/min using suction pump model F-18 (Fazzini Italy Code: F-18/2.00).

### 2.1. Liver mold

Because the phantom shape is important for diagnostic purposes, the commercial PVC liver mold of size 23 × 18 × 13 cm and weight 0.62 kg was used. The anterior surface consists of two lobes partially separated between them. The second surface representing the posterior liver surface displays the quadrate, caudate and gallbladder depressions. Both of the molds were formed using polyvinyl chloride (PVC) (Fig. 1).

### 2.2. Liver parenchyma and HCC samples

Different materials were used to fabricate the liver parenchyma and HCC. The parenchyma material consisted of 2.5 wt % of agarose powder (Hefei TNJ Chemical Industry Co.,Ltd.) as gelling agent; 2.6 wt % wax powder (Hefei TNJ Chemical Industry Co.,Ltd.); 2.6 wt % etherified hydroxyethyl cellulose (HEC) (Shin-Etsu Tylose R HS 100,000 YP2); 0.2 wt % benzalkonium chloride (BZK) (StepanguatR 50 NF) as anti-bacterial agent; 3.2 wt % propanediol (Dupont Zemea®) as a solvent; and the remaining component is water as volume spreader. The HCC samples were fabricated using 95 wt% of polyurethane and 5.0 wt% glycerol. Table 1 provides a summary for the material components used in the fabrication of the liver parenchyma and the HCC samples.

The liver parenchyma was prepared in three steps. The first step in the preparation of the liver parenchyma was through dissolving 2.6 g of HEC and 3.2 mL of propanediol in 100 mL of water. The solution was heated to 140 °C and stirred using a hot plate magnetic stirrer with magnetic steering at a maximum speed of 250 rotations/minute. The solution was allowed to cool below 100 °C before adding 0.2 mL BZK using a dropper. The solution was continuously stirred to prevent gravitational sedimentation of the HEC particles. Because of the

Table 1

Material components with the concentration of each material per weight used in preparing the liver parenchyma.

Material	Concentration	Notes
Agarose powder	2.5 wt %	HCC
Wax powder	2.6 wt %	
Hydroxyethylcellulose	2.6 wt %	
Benzalkonium Chloride	0.2 wt %	95 wt% polyurethane + 5 wt% glycerol
Propanediol	3.2 wt %	
Water	wt %	

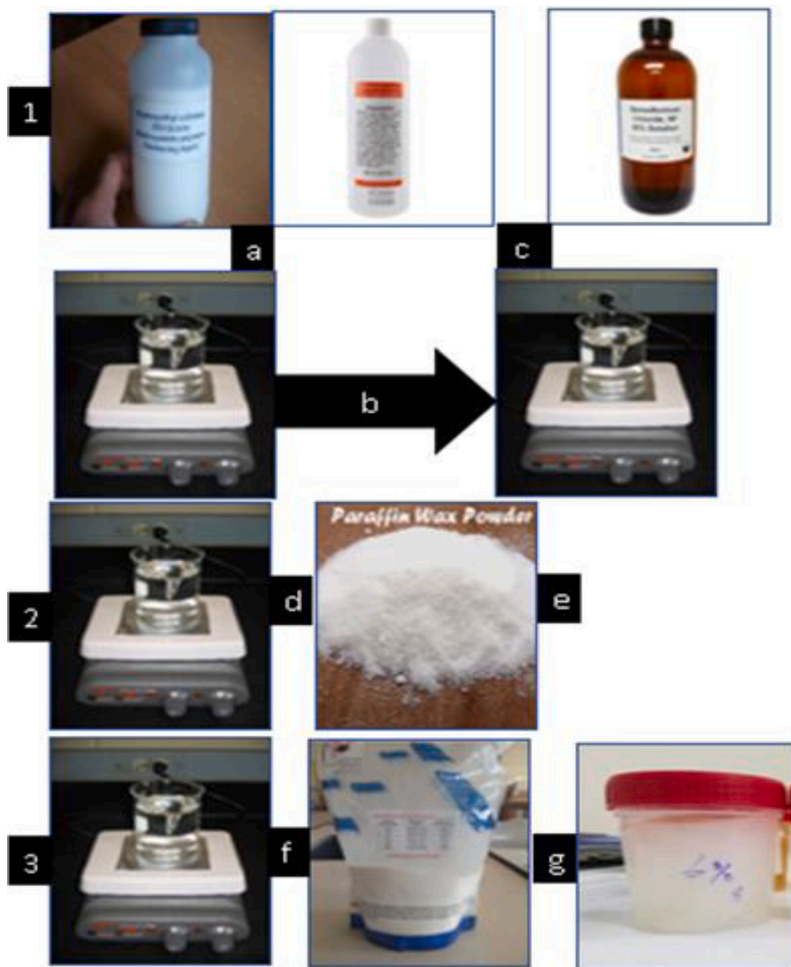


**Fig. 2.** Preparation steps of liver parenchyma made of agarose-wax mixture; (a): HEC powder and propanediol in 100 mL of water in the first beaker, heated to 140 °C; (b): The solution allowed to cool to 100 °C; (c): BZK added using a dropper; (d): Paraffin wax powder in 50 mL of water in a second beaker, heated to 90 °C; (e): cool first solution to 90 °C, add the wax solution; (f): agarose powder in 50 mL of water in a third beaker, heated to 50–60 °C; (g): second solution cooled to 60 °C and agarose solution added.

different melting points of agarose and HEC solution, the two solutions were prepared in separate glass beakers. The temperature was monitored using a digital thermometer (HI 98,501 Checktemp®). In the second step for agarose preparation, 2.5 g of agarose was dissolved in 50 mL of water. The water was placed in a flask on a magnetic stirrer and the agarose powder slowly added to the water while the solution was on the magnetic stirrer at a temperature of 50–60 °C. This was done to prevent agarose agglomeration.

The third stage was prepared by dissolving 2.6 g of paraffin wax powder in 50 mL of water. The solution was heated to 80–90 °C and continuously stirred to prevent gravitational sedimentation of the wax powder particles. Because of the different melting points of agarose and wax solution, the two solutions were prepared in separate glass beakers. Each beaker was heated at different temperatures until the agarose and wax had dissolved in solution. The agarose melting point reached 40–60 °C, whilst the wax dissolved at 40–90 °C.

The temperature was monitored using a digital thermometer. After the HEC mixture was cooled to a temperature of 90 °C, the wax solution was added while the solution was continuously stirred to prevent sedimentation of the HEC. The resultant solution was then allowed to cool below 60 °C before adding agarose solution while the solution was continuously stirred. Fig. 2 shows all of the preparation processes of the agarose-wax mixture.

In the three steps, the weight of the beakers were recorded before and after filling with the contents, so the content weight could be calculated. The mixture was shaken using a hot plate magnetic stirrer with magnetic stirring at maximum speed. Thus, the powder and any aggregates were broken up. The mixture remained in this situation for

30 min. The gel was created with clear and homogeneous components. After completing this step, the beaker was weighed again to calculate the loss of components in the processing steps. Any loss in weight was replaced with deionized water, and this addition was to ensure the solution consists of accurate material concentrations.

The solution was finally transferred and poured out into the liver mold and the resultant phantom kept for 12–24 hours at room temperature. The parenchyma can be stored at room temperature without cover but not for long. It can be stored for 7–10 days only. However, when using a container, it can be stored for 3–4 weeks. The phantom was covered well, using the same liver mold.

### 2.3. Flow mold (Blood vessels)

The flow mold consists of three parts as shown in Fig. 3. Because the study focused on the application of the dynamic phantom of HCC samples, the flow mold were conductive tubes - made of PVC - between the input part and the output part passing through the HCC samples which was inserted within the three cylinders. For this reason, the study did not focus on simulating the shape or size of blood vessels entering and leaving the liver -hepatic artery, hepatic vein and portal vein-, as much as the focus was on the function of these vessels, which is as a transport medium for materials entering and leaving the liver.

#### 2.3.1. Input part

The input part inside the phantom are three tubes made of similar materials to that used for the suction catheter. They are combined with each other in one syringe. Each tube is made of non-toxic PVC material,

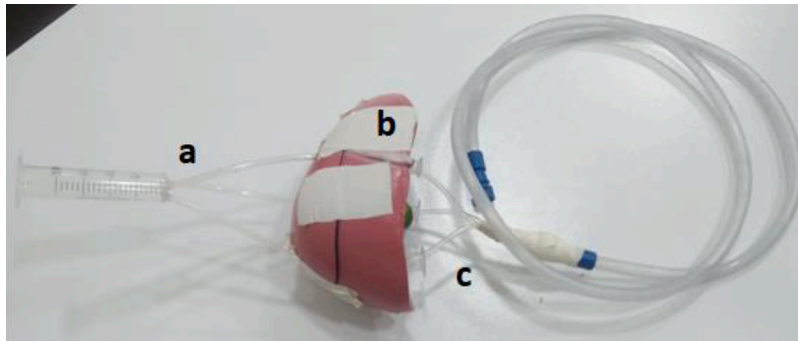


**Fig. 3.** The flow mold parts in the phantom; (a): the input part which is connected to the injector device; (b): the component which contains the cylindrical medium; and (c): the output part which is connected to the suction device.

10 cm in length and 14 F G in size, outer diameter of  $2.0 \pm 0.05$  mm, and thickness  $\geq 0.4$  mm. The large syringe was made of PVC material, and it has three holes in its head, thus, the three tubes entering the phantom can connect to it. Fig. 4 shows the construction of the input section.

### 2.3.2. Internal part (Cylindrical medium)

The second part of the flow phantom is the medium that connects the input tubes and the output tubes. This part is implanted into the phantom, and is made of three different sizes of acrylic cylinders; the first and second cylinders have a length of 7.5 cm and 9.6 mm in diameter; while the third cylinder has a length of 8.7 cm and diameter of 12.4 mm.

The upper part of the three cylinders consists of a small tip, thus the input tube can connect directly to it. The lower part of these cylinders is located outside of the phantom. It is used as an outlet and connected to the output tubes which are connected directly into the suction device. The cylindrical medium is shown in Fig. 5. Because the output orifices are placed out of the phantom, the different samples can be placed in the cylinders without affecting the internal components of the phantom. Therefore, the HCC sample with different sizes can be checked easily.

### 2.3.3. Output part

The outer part of the phantom consisted of three tubes which are similar to those of the three input tubes with the same diameter. The tip of each tube consists of a rubber closure implanted inside the cylinder to prevent fluid leakage inside the cylinder. This rubber closure can easily move inside the cylinder. The three tubes are connected to each other to form a single tube. Thus, it can be directly connected to the same suction tube (see Fig. 3).

## 2.4. Tumors

The phantom was integrated with different sizes of pathologic models, representative of HCC. These pathologies were placed in the cylinders inside the phantom. The location of the three lesions was near to the cylindrical tips which are connected directly to the input tubes. Therefore, when the CA is injected, the samples interact directly with this material.

### 2.4.1. Hepatocellular carcinoma

The HCC samples with different sizes; sample 1 (2 cm), sample 2 (1 cm) and sample 3 (0.5 cm) were used in this study. The basic material for HCC was made from 95 wt% polyurethane foam combined with 5 wt % glycerol (0.5 g glycerol /10 g of polyurethane). Because the samples were made of sponge polyurethane, the sample size was controlled by moving the rubber closure inside the cylinder to match the size of each sample.

## 2.5. Phantom assembly

The final structural design is shown in Fig. 3. The figure also shows the tube connections with the phantom. The parenchyma material was poured into the liver mold. The mixture was gently poured into the phantom to prevent air bubbles during the phantom preparation, with a spatula used to gently move the air bubbles towards the phantom container walls. The final phantom was assembled over 24 h.

Once cured, the phantom was placed and cooled at room temperature. Cooling steps are very important to make sure the mixture stays homogeneous without any cracks inside the phantom. To remove the phantom from the mold, the mold was divided and separated into



**Fig. 4.** The construction of the input part; three tubes connect to the large syringe.



Fig. 5. Cylindrical medium; (a): the near end of the input part; (b): the near end of the output part.

several parts. A spoon was used to remove the adhesion between the phantom and the mold wall.

## 2.6. Multimodal techniques

The phantom was applied under different imaging modalities (multimodal) including MRI, CT, and ultrasound techniques.

### 2.6.1. MRI

MR imaging was performed using a 1.5-T scanner (MAGNETOM Avanto, Siemens Healthcare, Erlangen, Germany) with a 48-radiofrequency channel system, which provides a maximum gradient strength of 45 m T/m and a peak slew rate of 200 m T/m/msec. 72 images were recorded, each with  $512 \times 512$  pixels. The field of view (FOV) read was 380 mm, FOV phase was 81.3 %, and the slice thickness was 3.0 mm.

The phantom underwent unenhanced imaging using both T2-weighted Half-Fourier Acquisition Single-shot Turbo Spin Echo (HASTE) and T1-weighted Volumetric Interpolated Breath-hold Examination (VIBE), and then the Dotarem contrast media was administered with a dose of 0.025 mmol per kilogram of phantom weight at a rate of 2 mL/sec through the input syringe. The Dotarem concentration was determined by dissolving 25 mL of Dotarem in 1000 mL of normal saline solution. Contrast medium administration was followed by a 20-mL saline flush at a rate of 2 mL/sec. T1-weighted three dimensional spoiled -VIBE- Dixon images were obtained at 25, 70, and 180 s after contrast medium injection, during the arterial, venous, and delayed phases, respectively.

### 2.6.2. CT

CT of the phantom was obtained with a 64 channel multi-detector row CT system (Brilliance iCT 64, Philips, Best, The Netherlands). The



Fig. 6. The appearance of the phantom after removing the mold.

protocol with  $512 \times 512$  pixels was acquired. The image resolution was  $0.5 \times 0.5$  mm, slice thickness was 0.6 mm, and the slice gapping between slices was 0.4 mm. A non-ionic CA telebrix, with flow rate 2 mL/sec, at a dose of 1.5 mL/kg (phantom weight) was used to obtain the dynamic enhancement scan for the phantom. The arterial phase image was obtained after 22 s from CA administration, venous phase after 50 s from the injection of the CA, and the delay (equilibrium) phase was obtained at 180 s after injection of the CA.

### 2.6.3. Ultrasound

Ultrasound images were gained using an Ultrasonix MDP scanner (Analogic Ultrasound, Canada). The images were recorded with attenuation at 3 MHz of 1 dB/cm/MHz, whereas at 5 MHz it was 2 dB/cm/MHz. Ultrasound images were taken by a radiologist with 8-year experience. The difference between HCC samples and liver parenchyma was decided by the radiologist.

## 3. Results

After the fabrication of the phantom was completed, the phantom mold was removed and the phantom appears as in Fig. 6. The figure shows the phantom after removing the mold from the phantom. Table 2 shows the characteristic proportions of the phantom.

The phantom was scanned under multimodal imaging using MRI, CT, and ultrasound. For assessment of the image quality, the differentiation between pathologies and normal liver parenchyma was approached.

### 3.1. MRI

Three readings were taken to determine the T1 and T2 signal intensities for liver parenchyma. The distribution of the three readings included most of the parenchyma to check for phantom homogeneity. Fig. 7 shows the reading locations inside the phantom. The average signal intensity of the three readings was calculated for the T1 image, which was 209, while it was estimated to be 360 in the T2 image.

The CA was applied to the different size HCC samples. Fig. 8 shows the result of CA enhancement through the HCC samples during MRI. It is observed that the samples of the first and second HCC samples were shown as hypointense (Fig. 8a) in the pre-phase before the CA was administered. In the late arterial phase, the samples show hyperintensity (Fig. 8b). Following that the two samples appeared less brilliantly in the porto-venous phase (partially washed) (Fig. 8c) and finally the two samples appeared in hypointense in the delay phase as complete

Table 2  
Characteristic proportions of the liver phantom.

Weight (gram)	1450
Volume (mL)	1198
Length (cm)	23
Width (cm)	18
Height (cm)	13

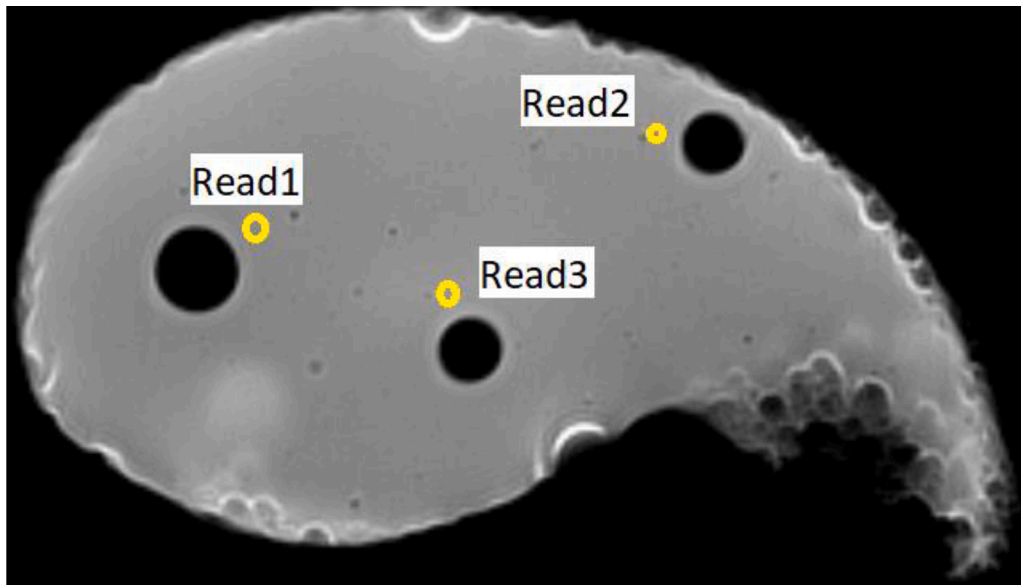


Fig. 7. T1 image of the phantom showing the axial cross section of the three cylindrical components where the tumor samples are located. Read 1, 2 and 3 represent the locations in the phantom where the T1 and T2 signal intensities were taken for the liver parenchyma.

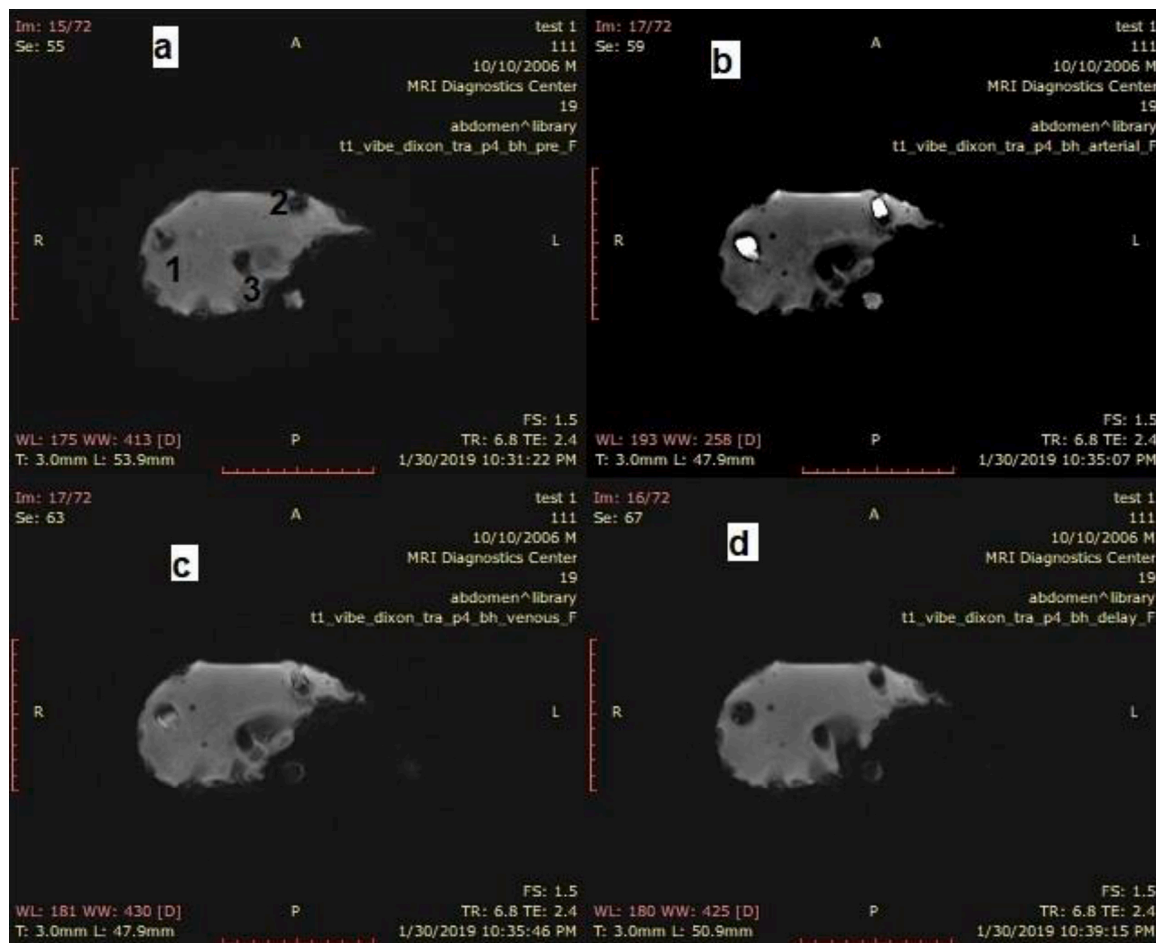
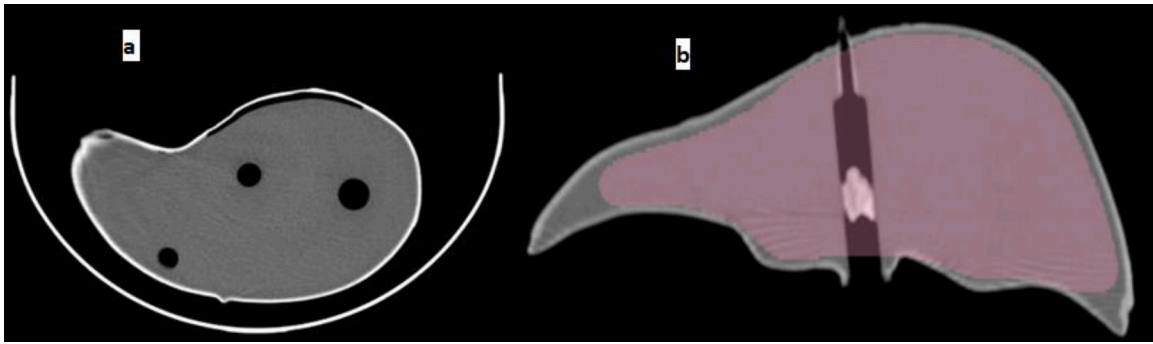


Fig. 8. T1-weighted -VIBE- Dixon images; (a): pre-contrast imaging; (b): arterial phase after 25 s (tumor is clearly bright); (c): venous phase after 70 s (tumor is slightly bright); and (d): delayed phase after 180 s (tumor clearly washout).



**Fig. 9.** CT imaging of gelatin-agar phantom; (a): axial cross section of the three cylindrical components containing the tumor samples; (b): coronal cross section of the phantom showing one sample inside the cylinder.



**Fig. 10.** CT axial images; (a): pre-contrast image; (b): arterial phase after 22 s (tumor is clearly bright); (c): venous phase after 50 s (tumor is slightly bright); and (d): delayed phase after 180 s (tumor clearly washed out).

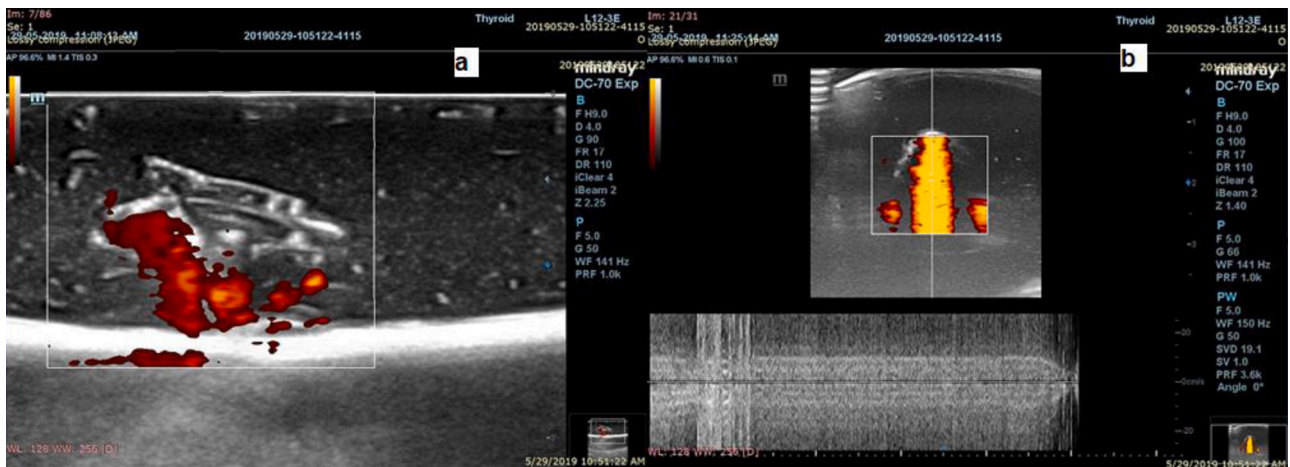


**Fig. 11.** Ultrasound images; (a): HCC appears hypoechoic compared with normal liver representing in red color dots; (b): color Doppler ultrasound of vessels with circulating fluid inside the sample (For interpretation of the references to colour in this figure legend, the reader is referred to the web version of this article).

washout (Fig. 8d). In all phases, the third sample (0.5 cm) does not appear.

### 3.2. CT

Fig. 9 shows the axial cross section (Fig. 9a) and the coronal section (Fig. 9b) of the phantom. In the figure the liver parenchyma tissue is clearly evident with a homogeneous texture. The Hounsfield unit (HU) for the parenchyma is distributed between 0–30 HU. The tumor models appeared with a heterogeneous texture. The pink color in Fig. 9b appeared after the coronal reconstruction of the images, and does not indicate any basic information that serves us in this regard.

After Telebrix 30 Meglumine (300 mg I/mL) injection in the phantom, the HU for the HCC appeared between 80 to 90 HU in the arterial phase 22 s after injection, 40–50 HU in the venous phase 50 s after injection, and 20–30 HU for the equilibrium phase 180 s after injection. Fig. 10 shows the result of contrast media enhancement through the sample in CT.

### 3.3. Ultrasound

Glycerol was added to both experiments to increase the contrast difference between HCC samples and liver parenchyma as seen in Fig. 11. In Fig. 11(a), the red dots in the image appear as the distribution of the HCC sample. The red color was used only to distinguish the HCC sample from the liver parenchyma. In Fig. 11(b), an orange color appears during the application of doppler-ultrasound on the HCC sample.

## 4. Discussion

The liver phantom was established successfully based on typical patterns of HCC. The project was motivated by the fact that there is no phantom described in the literature as far as we know which simulates the typical pattern of HCC. Where the typical pattern of HCC appears in its hyper arterial enhancement and delayed washout, washout in the portal venous phase is typically with malignant lesions of size greater than 2 cm, and this is what the previous studies showed [37–39].

This work was evaluated by a radiologist with eight years experience, through comparing the phantom results with real patient images. The results show that the parenchyma liver and HCC were well mimicked.

Referring to the actual liver weight, the study by Abogresha et al. [40] shows that the liver weight ranges between 1.2–1.6 kg. The results shown by the current study are consistent with this.

The signal intensity of T1 and T2 varies from device to device and from one sequence to another. The results of previous studies clearly show this difference [34,41–43]. In these studies, the signal intensity of T1 for liver ranged from 200 to 720 while signal intensity of T2 ranges between 40–80. Accordingly, the current results show that the signal intensity of T1 is an acceptable value when compared with previous studies, but for signal intensity of T2 there appeared to be a great difference between them, which is due to the percentage of water in the phantom.

In MRI, the first sample (HCC with size of 2 cm) and the second sample (HCC with size of 1 cm), appeared clearly in the resultant image after CA was applied, while the third sample (HCC with size of 0.5 cm), did not appear in any of the four phases. This result supports previous studies which highlighted the difficulty of detecting HCC in its early stages [15], because of their small size. The real reason this sample did not appear in MRI imaging is because of the use of the body coil which is designed to detect large organs such as the abdomen and spine within the human body. The organs in the abdomen for example help the device to determine the appropriate value of radiofrequency to be used to receive the signal intensity from the organs inside the body. However, because the manufactured phantom is not placed alongside other organs, the radiofrequency sent from the device will not be accurate as it

happens inside the human body. Therefore, some of the fine details in the image are missed like the small sized HCC samples.

In CT, previous studies show that the HU of the liver parenchyma is estimated to range between 40–50, while for HCC it appears to be in the range from 30 to 50 [44]. In the arterial stage, the HU value increases to 90 in HCC samples, and it returns to 60 in the venous phase, and finally reaches 40 in the equilibrium phase. The results of the current study corroborate what was obtained in the previous study, and accordingly it can be said that the manufactured phantom has succeeded in simulating the typical pattern of HCC under CT imaging.

To the best of our knowledge there are no commercial phantoms that mimic the flow part of HCC simulation such as the current liver phantom. However, the current phantom does not quite mimic blood vessels. They have been replaced with cylinders to allow for flow function. The major restrictions of the IOUSFAN® phantom are that they do not actually mimic tissue, do not simulate blood vessels, are rather expensive, and are also not a multimodal phantom. Widmann et al. have succeeded in developing phantoms by simulating realistic tumor shapes with the presence of blood vessel structures. However, they succeeded in designing a flexible phantom to evaluate only the CT system.

Multimodal liver phantoms were applied in a number of different previous studies [24,27,33,45]. Among these studies, only two phantoms presented by Rethy et al. [31] and Chmarra et al. [24] allow the combination of CT, ultrasound, and MRI modalities. Bazrafshan et al. [46] also prepared a liver-mimicking MRI gel phantom. They presented a phantom for temperature mapping for thermal tumor ablation, including radiofrequency ablation and laser induced interstitial thermotherapy. However, none of phantoms mentioned above provide HCC mimicry with blood flow functionality.

The major goal of the current study is to fabricate a liver phantom with HCC which fulfils various requirements in the same phantom; flow (functionality); multimodality; easy and standardized fabrication; and cheap. The current methodology can be applied to other large organs in the body such as the lung for bronchogenic carcinoma, stomach for the adenocarcinomas, and brain for different tumors like glioblastoma multiforme.

One of the limitations of the present study is the difficulty of representing breathing movements that affect real human liver under the components of the dynamic phantom. In addition, it is difficult to simulate the actual blood vessels of the liver in terms of shape and size, because the aim of the study revolves around the establishment of a dynamic phantom of HCC, and the blood vessels need special properties to use in the flow phantom [47–49]. In the future, there is a need to conduct studies to search for the properties of the current phantom, such as chemical, mechanical and electrical properties.

## 5. Conclusion

The method for producing HCC liver phantom has been established based on a typical HCC pattern including flow functionality. Multimodal phantom imaging has been applied. The phantom is adequate for diagnostic practice procedures and was prepared for technological system purposes. Even though the phantom simulated the blood vessels, it was unable to represent the small capillaries. Additional research is required to mimic a smaller size HCC with a flow system.

### Contributors

All authors contributed to the conception or design of the work, the acquisition, analysis, or interpretation of the data. All authors were involved in drafting and commenting on the paper and have approved the final version.

### Funding

This study did not receive any specific grant from funding agencies in

the public, commercial, or not-for-profit sectors.

## Disclosure

The author did not receive any type of commercial support in forms of either compensation or financial support for this study.

## Ethical approval

This article does not contain any studies with human participants or animals performed by any of the authors.

## Declaration of Competing Interest

The authors report no declarations of interest.

## Acknowledgements

This study was supported by the Ibn Rushd Radiology centre in Hebron West Bank.

## References

- K.M. Kee, J.H. Wang, C.M. Lee, C.L. Chen, C.S. Changchien, T.H. Hu, et al., Validation of clinical AJCC/UICC TNM staging system for hepatocellular carcinoma: analysis of 5,613 cases from a medical center in southern Taiwan, *Int. J. Cancer* 120 (12) (2007) 2650–2655, <https://doi.org/10.1002/ijc.22616>.
- Y. Nakamura, T. Kawaoka, T. Higaki, W. Fukumoto, Y. Honda, M. Iida, et al., Hepatocellular carcinoma treated with sorafenib: arterial tumor perfusion in dynamic contrast-enhanced CT as early imaging biomarkers for survival, *Eur. J. Radiol.* 98 (2018) 41–49, <https://doi.org/10.1016/j.ejrad.2017.10.017>.
- M.S. Ahmad, N. Suardi, A. Shukri, H. Mohammad, A.A. Oglat, B.M. Abunahel, et al., Current status regarding tumour progression, surveillance, diagnosis, staging, and treatment of HCC: a literature review, *J. Gastroenterol. Hepatol. Res.* 8 (2) (2019) 2841–2852, <https://doi.org/10.1111/j.1469-7580.2012.01495.x>.
- M. Soresi, A. Terranova, A. Licata, A. Serruto, G. Montalto, G. Brancatelli, L. Giannitrapani, Surveillance program for diagnosis of HCC in liver cirrhosis: role of ultrasound echo patterns, *Biomed Res. Int.* (2017) 2017, <https://doi.org/10.1155/2017/4932759>.
- D. Ippolito, G. Querques, S. Okolicsanyi, C.T. Franzesi, A. Pecorelli, S. Lombardi, et al., Dynamic contrast enhanced perfusion CT imaging: a diagnostic biomarker tool for survival prediction of tumour response to antiangiogenic treatment in patients with advanced HCC lesions, *Eur. J. Radiol.* 106 (2018) 62–68, <https://doi.org/10.1016/j.ejrad.2018.07.012>.
- E. Quai, Comparison between 80 kV, 100 kV and 120 kV CT protocols in the assessment of the therapeutic outcome in HCC, *Liver Pancreat Sci* 1 (1) (2016) 1–4, <https://doi.org/10.15761/LPS.1000101>.
- H. Toyoda, T. Kumada, T. Tada, Y. Sone, A. Maeda, Y. Kaneoka, Non-hypervascular hypointense nodules on Gd-EOB-DTPA-enhanced MRI as a predictor of outcomes for early-stage HCC, *Hepatol. Int.* 9 (1) (2015) 84–92, <https://doi.org/10.1007/s12072-014-9553-5>.
- S. Shankar, N. Kalra, A. Bhatia, R. Srinivasan, P. Singh, R.K. Dhiman, et al., Role of diffusion weighted imaging (DWI) for hepatocellular carcinoma (HCC) detection and its grading on 3T MRI: a prospective study, *J. Clin. Exp. Hepatol.* 6 (4) (2016) 303–310, <https://doi.org/10.1016/j.jceh.2016.08.012>.
- Y.J. Lee, J.M. Lee, J.S. Lee, H.Y. Lee, B.H. Park, Y.H. Kim, et al., Hepatocellular carcinoma: diagnostic performance of multidetector CT and MR imaging—a systematic review and meta-analysis, *Radiology* 275 (1) (2015) 97–109, <https://doi.org/10.1148/radiol.14140690>.
- R.F. Hanna, V.Z. Miloushev, A. Tang, L.A. Finklestone, S.Z. Brejt, R.S. Sandhu, et al., Comparative 13-year meta-analysis of the sensitivity and positive predictive value of ultrasound, CT, and MRI for detecting hepatocellular carcinoma, *Abdom. Radiol.* 41 (1) (2016) 71–90, <https://doi.org/10.1007/s00261-015-0592-8>.
- M.T. Lin, C.C. Wang, Y.F. Cheng, H.L. Eng, Y.H. Yen, M.C. Tsai, et al., Comprehensive comparison of multiple-detector computed tomography and dynamic magnetic resonance imaging in the diagnosis of hepatocellular carcinoma with varying degrees of fibrosis, *PLoS One* 11 (11) (2016), e0166157, <https://doi.org/10.1371/journal.pone.0166157>.
- Computerized Imaging Reference Systems, Inc. (2017) CIRS, Triple modality 3D abdominal phantom, Model 057A. <http://www.cirsinc.com/products/modality/6/5/triple-modality-3d-abdominal-phantom/>. Accessed 20 June 2020.
- Kyoto Kagaku Co., Ltd, IOUSFAN, Abdominal Intraop- Erative & Laparoscopic Ultrasound Phantom, 2017, p. 2017. Accessed 20 June 2020, <http://www.kyotokagaku.com/products/detail03/us-3.html>.
- Semianthropomorphic Liver Phantom, “QRM-Liver-Phantom,” [http://www.qrm.de/content/products/anthropomorphic/liver\\_phantom.htm](http://www.qrm.de/content/products/anthropomorphic/liver_phantom.htm). Accessed 20 June 2020.
- M.S. Ahmad, N. Suardi, A. Shukri, H. Mohammad, A.A. Oglat, A. Alarab, O. Makhamrah, Chemical characteristics, motivation and strategies in choice of materials used as liver phantom: a literature review, *Ultrasound* 28 (1) (2020) 7, <https://doi.org/10.4103/JMU.JMU.4.19>.
- A.T. Martinsen, H.K. Sæther, D.R. Olsen, P. Skaane, H.M. Olerud, Reduction in dose from CT examinations of liver lesions with a new postprocessing filter: a ROC phantom study, *Acta radiol.* 49 (3) (2008) 303–309, <https://doi.org/10.1080/02841850701793769>.
- M.E. Baker, F. Dong, A. Primak, N.A. Obuchowski, D. Einstein, N. Gandhi, et al., Contrast-to-noise ratio and low-contrast object resolution on full-and low-dose MDCT: SAFIRE versus filtered back projection in a low-contrast object phantom and in the liver, *Am. J. Roentgenol.* 199 (1) (2012) 8–18, <https://doi.org/10.2214/AJR.11.7421>.
- S.T. Schindera, J.C. Torrente, T.D. Ruder, H. Hoppe, D. Marin, R.C. Nelson, Z. Szucs-Farkas, Decreased detection of hypovascular liver tumors with MDCT in obese patients: a phantom study, *Am. J. Roentgenol.* 196 (6) (2011) W772–W776, <https://doi.org/10.2214/AJR.10.5351>.
- K.S. Kim, J.M. Lee, S.H. Kim, K.W. Kim, S.J. Kim, S.H. Cho, et al., Image fusion in dual energy computed tomography for detection of hypervascular liver hepatocellular carcinoma: phantom and preliminary studies, *Invest. Radiol.* 45 (3) (2010) 149–157, <https://doi.org/10.1097/RLI.0b013e3181d32119>.
- N. Shevchenko, B. Seidl, J. Schwaiger, M. Markert, T.C. Lueth, MiMed liver: a planning system for liver surgery, in: In 2010 Annual International Conference of the IEEE Engineering in Medicine and Biology, IEEE, 2010, pp. 1882–1885, <https://doi.org/10.1109/IEMBS.2010.5627120>.
- G. Widmann, D. Wallach, G. Toporek, P. Schullian, S. Weber, R. Bale, Angiographic C-Arm CT-versus MDCT-Guided stereotactic punctures of liver lesions: nonrigid phantom study, *Am. J. Roentgenol.* 201 (5) (2013) 1136–1140, <https://doi.org/10.2214/AJR.12.10405>.
- E. Joe, S.H. Kim, K.B. Lee, J.J. Jang, J.Y. Lee, J.M. Lee, et al., Feasibility and accuracy of dual-source dual-energy CT for noninvasive determination of hepatic iron accumulation, *Radiology* 262 (1) (2012) 126–135, <https://doi.org/10.1148/radiol.11110060/-DC1>.
- M. Kazuhiro, N. Kawai, M. Sato, H. Minamiguchi, M. Nakai, T. Sonomura, et al., Optimum CT reconstruction parameters for vascular and hepatocellular carcinoma models in a liver phantom with multi-level dynamic computed tomography with 64 detector rows: a basic study, *Radiol. Phys. Technol.* 6 (2) (2013) 317–325, <https://doi.org/10.1007/s12194-013-0203-8>.
- M.K. Chmarra, R. Hansen, R. Märvik, T. Langø, Multimodal phantom of liver tissue, *PLoS One* 8 (5) (2013) e64180, <https://doi.org/10.1371/journal.pone.0064180>.
- E. In, H.E. Naguib, M. Haider, Mechanical stability analysis of carrageenan-based polymer gel for magnetic resonance imaging liver phantom with lesion particles, *J. Med. Imaging* 1 (3) (2014), 035502, <https://doi.org/10.1117/1.JMI.1.3.035502>.
- M.A. Rube, A.B. Holbrook, B.F. Cox, R. Buciu, A. Melzer, Wireless mobile technology to improve workflow and feasibility of MR-guided percutaneous interventions, *Int. J. Comput. Assist. Radiol. Surg.* 10 (5) (2015) 665–676, <https://doi.org/10.1007/s11548-014-1109-6>.
- N. Shevchenko, J. Schwaiger, M. Markert, W. Flatz, T.C. Lueth, Evaluation of a resectable ultrasound liver phantom for testing of surgical navigation systems, in: In 2011 Annual International Conference of the IEEE Engineering in Medicine and Biology Society, IEEE, 2011, pp. 916–919, <https://doi.org/10.1109/IEMBS.2011.6090205>.
- A. Pacioni, M. Carbone, C. Freschi, R. Vigliani, V. Ferrari, M. Ferrari, Patient-specific ultrasound liver phantom: materials and fabrication method, *Int. J. Comput. Assist. Radiol. Surg.* 10 (7) (2015) 1065–1075, <https://doi.org/10.1007/s11548-014-1120-y>.
- J. Schwaiger, M. Markert, N. Shevchenko, T.C. Lueth, The effects of real-time image navigation in operative liver surgery, *Int. J. Comput. Assist. Radiol. Surg.* 6 (6) (2011) 785–796, <https://doi.org/10.1007/s11548-011-0557-5>.
- K. Sugimoto, F. Moriyasu, J. Shiraishi, M. Yamada, Y. Imai, A phantom study comparing ultrasound-guided liver tumor puncture using new real-time 3D ultrasound and conventional 2D ultrasound, *Am. J. Roentgenol.* 196 (6) (2011) W753–W757, <https://doi.org/10.2214/AJR.10.5552>.
- A. Rethy, J.O. Sæternes, J. Halgunset, R. Märvik, E.F. Hofstad, J.A. Sánchez-Margallo, T. Langø, Anthropomorphic liver phantom with flow for multimodal image-guided liver therapy research and training, *Int. J. Comput. Assist. Radiol. Surg.* 13 (1) (2018) 61–72, <https://doi.org/10.1007/s11548-017-1669-3>.
- F. Nazem, A. Ahmadian, N.D. Seraj, M. Giti, Two-stage point-based registration method between ultrasound and CT imaging of the liver based on ICP and unscented Kalman filter: a phantom study, *Int. J. Comput. Assist. Radiol. Surg.* 9 (1) (2014) 39–48, <https://doi.org/10.1007/s11548-013-0907-6>.
- Y.H. Kao, O.S. Luddington, S.R. Culleton, R.J. Francis, J.A. Boucek, A gelatin liver phantom of suspended 90Y resin microspheres to simulate the physiologic microsphere biodistribution of a postradioembolization liver, *J. Nucl. Med. Technol.* 42 (4) (2014) 265–268, <https://doi.org/10.2967/jnm.114.145292>.
- H. Kato, M. Kuroda, K. Yoshimura, A. Yoshida, K. Hanamoto, S. Kawasaki, et al., Composition of MRI phantom equivalent to human tissues, *Med. Phys.* 32 (10) (2005) 3199–3208, <https://doi.org/10.1118/1.2047807>.
- R. Javan, M.N. Zeman, A prototype educational model for hepatobiliary interventions: unveiling the role of graphic designers in medical 3D printing, *J. Digit. Imaging* 31 (1) (2018) 133–143, <https://doi.org/10.1007/s10278-017-0012-4>.
- K. Knox, C.W. Kerber, S.A. Singel, M.J. Bailey, S.G. Imbesi, Stereolithographic vascular replicas from CT scans: choosing treatment strategies, teaching, and research from live patient scan data, *Am. J. Neuroradiol.* 26 (6) (2005) 1428–1431, <https://doi.org/10.1146/annurev-anchem-061417-125935>.
- M.S. Ahmad, N. Suardi, A. Shukri, N.N.A.N. Ab Razak, A.A. Oglat, H. Mohammad, A recent short review in non-invasive magnetic resonance imaging on assessment

- of HCC stages: MRI findings and pathological diagnosis, *J. Gastroenterol. Hepatol. Res.* 9 (2) (2020) 3113–3123.
- [38] M.H. Choi, J.I. Choi, Y.J. Lee, M.Y. Park, S.E. Rha, C. Lall, MRI of small hepatocellular carcinoma: typical features are less frequent below a size cutoff of 1.5 cm, *Am. J. Roentgenol.* 208 (3) (2017) 544–551, <https://doi.org/10.2214/AJR.16.16414>.
- [39] D. Ippolito, R. Inchingolo, L. Grazioli, S.G. Drago, M. Nardella, M. Gatti, R. Faletti, Recent advances in non-invasive magnetic resonance imaging assessment of hepatocellular carcinoma, *World J. Gastroenterol.* 24 (23) (2018) 2413, <https://doi.org/10.3748/wjg.v24.i23.2413>.
- [40] N.M. Abogresha, M.A. Hussain, R. Hassan, D. A El-Tamany, Rebound weight gain worsen the experimental NonAlcoholic fatty liver disease in rats, *Suez Canal University Medical Journal* 18 (1) (2015) 16–29, <https://doi.org/10.21608/scumj.2015.43983>.
- [41] P.A. Bottomley, C.J. Hardy, R.E. Argersinger, G. Allen-Moore, A review of 1H nuclear magnetic resonance relaxation in pathology: are T1 and T2 diagnostic? *Med. Phys.* 14 (1) (1987) 1–37, <https://doi.org/10.1118/1.596111>.
- [42] K. Yoshimura, H. Kato, M. Kuroda, A. Yoshida, K. Hanamoto, A. Tanaka, et al., Development of a tissue-equivalent MRI phantom using carrageenan gel, *Magnetic Resonance Med. Off. J. Int. Soc. Magnetic Resonance Med.* 50 (5) (2003) 1011–1017, <https://doi.org/10.1002/mrm.10619>.
- [43] C.M. De Bazelaire, G.D. Duhamel, N.M. Rofsky, D.C. Alsop, MR imaging relaxation times of abdominal and pelvic tissues measured in vivo at 3.0 T: preliminary results, *Radiology* 230 (3) (2004) 652–659, <https://doi.org/10.1148/radiol.2303021331>.
- [44] T. Hennemig, Z.J. Yang, C.K. Ong, S.K. Venkatesh, Utility of non-contrast-enhanced CT for improved detection of arterial phase hyperenhancement in hepatocellular carcinoma, *Abdom. Imaging* 39 (6) (2014) 1247–1254, <https://doi.org/10.1007/s00261-014-0174-1>.
- [45] P. Bao, J. Warmath, R. Galloway, A. Herline, Ultrasound-to-computer-tomography registration for image-guided laparoscopic liver surgery, *Surgical Endoscopy Other Interventional Techniques* 19 (3) (2005) 424–429, <https://doi.org/10.1007/s00464-004-8902-1>.
- [46] B. Bazrafshan, F. Hübner, P. Farshid, M.C. Larson, V. Vogel, W. Mäntele, T.J. Vogl, A liver-mimicking MRI phantom for thermal ablation experiments, *Med. Phys.* 38 (5) (2011) 2674–2684, <https://doi.org/10.1118/1.3570577>.
- [47] A.A. Oqlat, M.Z. Matjafri, N. Suardi, M.A. Oqlat, M.A. Abdelrahman, A.A. Oqlat, et al., Chemical items used for preparing tissue-mimicking material of wall-less flow phantom for doppler ultrasound imaging, *J. Med. Ultrasound* 26 (3) (2018) 123, doi: PMC6159330.
- [48] A.O. Ammar, M.Z. Matjafri, N. Suardi, M.A. Oqlat, A.A. Oqlat, M.A. Abdelrahman, et al., Characterization and construction of a robust and elastic wall-less flow phantom for high pressure flow rate using Doppler ultrasound applications, *Nat. Eng. Sci.* 3 (3) (2018) 359–377, <https://doi.org/10.28978/nesciences.468972>.
- [49] A.A. Oqlat, M. Alshipli, M.A. Sayah, M.S. Ahmad, Artifacts in Diagnostic Ultrasonography, 2020, <https://doi.org/10.1177/1544316720923937>.